Research Square

Preprints are preliminary reports that have not undergone peer review.
They should not be considered conclusive, used to inform clinical practice,
or referenced by the media as validated information.

Curvature-Controlled Instability Coupling in Hypersonic Three-Dimensional Boundary-Layer Transition

Yatian Zhao
Central South University
Xianda Zeng
Central South University
Jian Luo
Central South University
Fanzhi Zeng
Central South University
Ze Pang
Central South University
Hongkang Liu
liuhongkang@csu.edu.cn

Central South University

Article

Keywords: Lifting-Body, Hypersonic Transition, Multimode Instability, Curvature Gradient, Heat Flux

Posted Date: June 10th, 2026

DOI: https://doi.org/10.21203/rs.3.rs-9826495/v1

License: This work is licensed under a Creative Commons Attribution 4.0 International License.
Read Full License

Additional Declarations: No competing interests reported.

Version of Record: A version of this preprint was published at Scientific Reports on August 27th, 2026.
See the published version at https://doi.org/10.1038/s41598-026-67520-y.

Curvature-Controlled Instability Coupling in Hypersonic Three-Dimensional Boundary-Layer Transition

Yatian Zhao[1,2,3], Xianda Zeng [1,2,3], Jian Luo[4], Fanzhi Zeng[4], Ze Pang [1,2,3], Hongkang Liu[1,2,3,a]

(1. Extreme Flow Energy Frontier Science Center, Central South University, Changsha 410075, China

2. School of Traffic & Transportation Engineering, Central South University, Changsha 410075, China

3. Key Laboratory of Traffic Safety on Track Ministry of Education, Central South University, Changsha 410007, China

4. National Key Laboratory of High-Efficiency Reusable Aerospace Transportation Technology, Changsha 410075, China

a. Corresponding author: **liuhongkang@csu.edu.cn**)

Abstract: Boundary-layer transition on hypersonic lifting bodies is strongly affected by three-dimensional effects and surface curvature, which influence instability development and aerodynamic heating. However, the specific role of curvature in modulating transition behavior remains not fully characterized.

This study investigates the effect of geometric curvature on transition mechanisms using a parameterized lifting-body configuration. Variations in concave and convex curvature are introduced to examine their influence on pressure distribution, boundary-layer structure, and instability interaction. Simulations are performed using an improved k–ω–γ transition model. Results show that curvature modifies the circumferential pressure gradient and boundary-layer thickness, leading to significant changes in dominant instability modes and transition patterns. Increasing concave curvature promotes the interaction between crossflow and streamwise instabilities, resulting in a shift from single- to double-cone transition structures. Changes in convex curvature produce non-monotonic variations in transition behavior, including switching between different dominant mechanisms and corresponding transition-front shapes.

These results demonstrate that geometric curvature provides an effective means of controlling transition behavior and offers practical guidance for the aerodynamic design of hypersonic vehicles.

Keywords： Lifting-Body, Hypersonic Transition, Multimode Instability, Curvature Gradient, Heat Flux

1 Introduction：

Under hypersonic flight conditions (Ma > 5), boundary-layer transition from laminar to turbulent flow represents one of the most critical processes governing the aerodynamic and thermal environments of high-speed vehicles[1]. The onset of transition leads to abrupt increases in surface heat flux and skin friction, significantly affecting thermal protection requirements, structural integrity, and vehicle performance. Hufgard et al. [2] found that heat-flux-controlled transpiration cooling can adaptively regulate coolant mass flow under extreme heating conditions, highlighting the importance of accurately predicting transition-induced heat-flux variations for hypersonic thermal-protection design. In practical hypersonic vehicles, boundary layers develop over highly three-dimensional geometries characterized by swept leading edges, curved surfaces, and varying cross-sectional contours. These geometric features generate strong pressure gradients that fundamentally modify boundary-layer development and instability characteristics. As a result, transition in realistic hypersonic flows rarely arises from a single instability mechanism but instead emerges from the interaction and competition among several types of disturbances, including first-mode instability, second-mode instability, crossflow instability, and non-modal streamwise streaks. Here, the first and second modes refer to modal instability waves associated with viscous/inviscid and acoustic-type mechanisms, respectively; crossflow instability denotes steady or traveling crossflow modes induced by spanwise pressure gradients; and streamwise streaks refer to elongated low- and high-speed regions generated by non-modal transient growth rather than a separate modal instability with streamwise vorticity.

The instability physics of hypersonic boundary layers has traditionally been investigated through canonical configurations designed to isolate individual mechanisms. Early theoretical and experimental studies on sharp and blunt cones established second-mode instability as the dominant transition mechanism at high Mach numbers and revealed the non-monotonic influence of nose bluntness. Kim et al.[3] found that nose-tip bluntness delayed transition onset and shifted the dominant second-

mode instability to lower frequencies, indicating that bluntness can regulate hypersonic transition by modifying instability characteristics. Chen et al. [4]summarized these studies and highlighted the importance of shock-induced receptivity in generating unstable disturbances in hypersonic boundary layers. Flight-test investigations of hypersonic transition vehicles have shown that the transition location in real flight is highly sensitive to surface imperfections and environmental disturbances[],[6],. Direct numerical simulations by Guo et al.[7] revealed a nonmodal transition pathway in which streamwise streaks generated near the leading edge undergo secondary instability and subsequently evolve into turbulent spots. Recent studies further indicate that multiple disturbance mechanisms may coexist and interact during transition. For example, Li [8]demonstrated that high-frequency instability waves and streamwise streaks structures can coexist and jointly contribute to transition development in hypersonic boundary layers. Based on the findings of Goparaju[9] and Paredes[10], the entropy layer generated by nose bluntness may suppress classical Mack-mode instabilities while promoting the amplification of streamwise streaks, leading to alternative transition pathways in blunt leading-edge configurations.

As investigations expanded to three-dimensional geometries, crossflow instability emerged as a key mechanism governing transition in swept or curved configurations. Experiments and simulations by Qiu et al.[11] showed that traveling crossflow vortices may interact with second-mode disturbances and promote secondary instabilities. Paredes and Theofilis[12] identified centerline instabilities associated with low-velocity streaks as well as oblique second-mode disturbances in the boundary layer over the HIFiRE-5 elliptic cone. Malik[13] demonstrated that crossflow vortices can dominate transition in swept high-speed boundary layers when strong spanwise pressure gradients are present. Direct numerical simulations have shown that freestream acoustic disturbances can interact with intrinsic instability modes in hypersonic boundary layers, and nonlinear interactions among multiple modes may accelerate transition[],[15].

To bridge the gap between canonical studies and realistic flight geometries, several quasi-realistic benchmark configurations have been developed over the past two decades. The HIFiRE-5 elliptic cone provides a controlled configuration for investigating crossflow instability in three-dimensional hypersonic boundary layers[16]. Stability analyses of the BOLT configuration indicated that stationary crossflow disturbances are the dominant breakdown mechanism away from the centerline and

leading edge[17]. The HyTRV lifting-body configuration was introduced to reproduce the asymmetric transition behavior typical of lifting vehicles. Qi et al. [18]reported multiple transition zones in hypersonic lifting-body boundary layers arising from crossflow instability and separation-induced secondary instability. Experimental investigations further showed that different instability mechanisms may dominate on the windward and leeward sides of three-dimensional configurations[19]. Wind-tunnel visualizations, together with stability analysis and model predictions by Xiang et al.[20], showed that circumferential pressure gradients strongly influence cross-flow development and the distribution of transition zones on the HyTRV lifting body.

In parallel with these fundamental studies, considerable effort has been devoted to the development of engineering transition models capable of predicting laminar–turbulent transition in high-speed flows. The correlation-based γ–$Re\theta$ transition model proposed by Langtry and Menter[21] introduced transport equations for intermittency and transition momentum thickness Reynolds number, enabling transition prediction within the RANS framework. Building upon this concept, the k–ω–γ transition model incorporates instability time-scale analysis to account for the effects of first-mode, second-mode, and crossflow disturbances in hypersonic boundary layers. Subsequent studies extended this framework to complex high-speed configurations. For example, Zhou et al.[22] introduced corrections for Reynolds-number effects and second-mode instability, improving transition prediction for hypersonic vehicles such as X-33 and X-51A. Zhao et al.[23] introduced a separation-induced intermittency correction to improve the prediction of transition in separated hypersonic flows. In addition, recent studies have explored active control strategies for hypersonic transition. Oz and Kara [24] demonstrated that localized cooling combined with metasurface treatments can significantly suppress disturbance growth, highlighting the potential of surface-based mechanisms in regulating transition behavior.

In three-dimensional hypersonic boundary layers, curvature-induced pressure gradients drive crossflow motion, redistribute boundary-layer thickness, and modify the relative amplification of first-mode, second-mode, and crossflow instabilities. Variations in geometric curvature may therefore reorganize modal dominance and reshape transition-front topology. Despite the recognized importance of curvature effects, a systematic framework that isolates curvature-driven instability interaction is still lacking. The central physical question is therefore how geometric curvature

regulates the competition among disturbance mechanisms and governs the emergence of coupled-instability behavior in three-dimensional hypersonic boundary layers.

To address this problem, the present study investigates curvature-controlled instability interaction in a hypersonic lifting-body boundary layer within the *k–ω–γ* transition modeling framework. A parametric configuration is constructed in which concave and convex curvature can be varied independently while preserving the essential features of realistic three-dimensional hypersonic flows. Within this framework, the evolution of instability time scales, crossflow intensity, and transition-front development is systematically examined to clarify how curvature gradients regulate the competition among disturbance mechanisms and shape multimode transition behavior.

2 Numerical Methodology

The numerical simulations in this study are performed using an in-house solver developed by the authors' research group. The solver is based on the finite-volume method to solve the Reynolds-averaged Navier–Stokes (RANS) equations. The inviscid fluxes are discretized using the Roe approximate Riemann scheme with flux-difference splitting, while the viscous fluxes are computed using a second-order central difference scheme. Time integration is carried out using an implicit LU-SGS method, and boundary-layer transition is predicted using an improved *k–ω–γ* transition model. For the boundary conditions, the configuration surface is treated as a no-slip isothermal wall, and owing to the compressible nature of the flow, the outer boundaries of the computational domain are specified as pressure far-field conditions.

2.1 Improved *k–ω–γ* Transition Model

The improved *k–ω–γ* model adopted in this study is developed on the basis of the *k–ω–γ* transition model proposed by Wang and Fu et al. [],[],[29], which consists of three transport equations for the turbulent kinetic energy k, the specific dissipation rate of turbulent kinetic energy ω, and the intermittency factor γ, and can be expressed as follows:

$$\frac{\partial(\rho k)}{\partial t}+\frac{\partial(\rho \mu_j k)}{\partial x_j}=\frac{\partial}{\partial x_j}\left[\left(\mu+\sigma_k \mu_{eff}\right)\frac{\partial k}{\partial x_j}\right]+P_k(\gamma)-D_k \tag{2.1}$$

$$\frac{\partial(\rho\omega)}{\partial t}+\frac{\partial(\rho\mu_j\omega)}{\partial x_j}=\frac{\partial}{\partial x_j}\left[\left(\mu+\sigma_\omega\mu_{eff}\right)\frac{\partial\omega}{\partial x_j}\right]+P_\omega-D_\omega+Cd_\omega \tag{2.2}$$

$$\frac{\partial(\rho\gamma)}{\partial t}+\frac{\partial(\rho\mu_j\gamma)}{\partial x_j}=\frac{\partial}{\partial x_j}\left[\left(\mu+\sigma_\gamma\mu_{eff}\right)\frac{\partial\gamma}{\partial x_j}\right]+P_\gamma-D_\gamma \tag{2.3}$$

Here, the transport equations for the turbulent kinetic energy k and the specific dissipation rate ω are identical to those of the SST turbulence model, except that the eddy viscosity μ_t is replaced by the effective viscosity μ_{eff}; in addition, C is a constant, d denotes the distance to the wall, μ_{eff} represents the effective viscosity, and P_γ and D_γ are the production and destruction terms of the intermittency factor, respectively, whose expressions are given as follows:

$$P_\gamma=C_4\rho F_{\text{onset}}\sqrt{-ln(1-\gamma)}\left[1+C_5\sqrt{\frac{k}{2E_u}}\right]\frac{d}{\nu}|\nabla E_u|, D_\gamma=\gamma P_\gamma \tag{2.4}$$

$$F_{\text{onset}}=1-exp\left(-C_6\frac{\zeta_{\text{eff}}\sqrt{k}\,|\nabla k|}{\nu|\nabla E_u|}\right) \tag{2.5}$$

$$\mu_{eff}=(1-\gamma)\mu_{nt}+\gamma\mu_t \tag{2.6}$$

In the above equations, $E_u=0.5|U|^2$ denotes the kinetic energy of the mean flow, μ_{nt} is the non-turbulent fluctuation viscosity, and μt is the turbulent fluctuation viscosity. It is readily observed that when γ=0, μ_{eff}=μ_{nt}, indicating a laminar flow state that nevertheless accounts for the effects of non-turbulent fluctuations. When γ=1, μ_{eff}=μ_t, and the transition formulation reduces to the standard SST turbulence model. For 0<γ<1, the flow is in a transitional state. The modeling of the non-turbulent fluctuation viscosity μ_{nt} is analogous to that of the eddy viscosity and is given by the following expression:

$$\mu_{nt}=C_\mu\rho k\tau_{nt} \tag{2.7}$$

In this expression, C_μ is a model constant, k denotes the total fluctuation kinetic energy, and τ_{nt} represents the non-turbulent fluctuation time scale, which is defined as follows:

$$\tau_{nt}=\begin{cases}\tau_{nt1}+\tau_{cross} & |Ma_{rel}|\le 1\\ \tau_{nt1}+\tau_{nt2}+\tau_{cross} & |Ma_{rel}|>1\end{cases} \tag{2.8}$$

The time scales of the first and second modes are denoted by τ_{nt1} and τ_{nt2}, respectively, while τ_{cross} represents the crossflow-mode time scale that characterizes crossflow effects. It should be noted that τ_{nt2} contributes to the transition process only

when the relative Mach number $|Ma_{rel}|>1$. The expressions for τ_{nt1}, τ_{nt2}, and τ_{cross} are given as follows:

$$\tau_{nt1} = C_3 \frac{\zeta_{eff}^{1.5}}{\sqrt{\sqrt{2Eu}\,\frac{\mu}{\rho}}} \tag{2.9}$$

$$\tau_{nt2} = C_4 \frac{2\zeta_{eff}}{U(y_s)} \tag{2.10}$$

$$\tau_{cross} = C_5 \frac{\zeta_{eff}}{U_e} f(w) f\left(Re_{cf}\right) \tag{2.11}$$

In this formulation, C_3, C_4, and C_5 denote constant model parameters, while ζ_{eff} represents the effective length scale. $U(y_s)$ is the velocity at the generalized inflection point y_s, and Ue is the local velocity at the edge of the boundary layer. w denotes the crossflow velocity, and Re_{CF} is the crossflow Reynolds number. It should be noted that Eqs. (2.9)–(2.11) explicitly define the instability time scales associated with the first mode, the second mode, and the crossflow mode, respectively. Non-modal streamwise streaks are not introduced as an additional fourth time-scale term in the present transition model. Instead, their influence is considered indirectly through the mean-flow distortion, boundary-layer thickening, and local modification of the first-mode and crossflow-related time scales. Therefore, in the following analysis, the term "streamwise streaks" is used only to describe the streak-like mean-flow structures observed in the boundary layer, rather than an explicitly modeled modal instability.

For detailed information on the modeling methodology of the improved k–ω–γ model and the numerical discretization of its governing equations, refer to references [],[],[27].

2.2 Case Validation

To validate the applicability and reliability of the improved k–ω–γ transition model for predicting complex three-dimensional hypersonic flows, two hypersonic vehicle configurations with well-documented experimental data and representative flow features—namely, the HyTRV and HIFiRE-5—are selected as benchmark cases. By systematically comparing the numerical simulation results with authoritative published experimental data, the model's capability to predict transition onset locations, transition surfaces, and overall flow structures is evaluated, thereby providing a reliable foundation for subsequent parametric configuration studies.

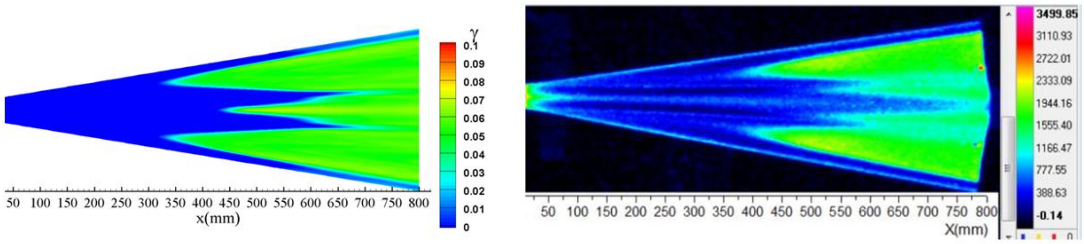
2.2.1 HyTRV

For the leeward surface of the HyTRV configuration, Fig. 1 (a) presents the numerical predictions obtained using the improved k–ω–γ transition model, while Fig. 1 (b) shows the wall heat-rise distribution measured in the wind tunnel of the National Key Laboratory of Aerospace Aerodynamics under identical freestream conditions , the details of which are listed in Table 1(unpublished data). The comparison indicates that the simulation satisfactorily reproduces the primary characteristics of the transition process, including the onset location situated between the centerline and the side edges at approximately $x/L \approx 44$. Overall, the predicted transition topology exhibits good agreement with the experimental observations, suggesting that the model captures the dominant features governing transition development over the leeward surface of the HyTRV configuration.

Nevertheless, noticeable discrepancies remain near the centerline. In the numerical result, the intermittency factor γ is relatively high along the centerline, suggesting an early transition tendency predicted by the model. In contrast, the experimental heat-rise image shows a comparatively weak heat-flux increase in the centerline region. This difference may arise from the fact that the numerical result is evaluated using the intermittency factor, whereas the experiment visualizes the wall heat-flux response; these two quantities are related but not strictly equivalent. In addition, the present RANS-based transition model may overpredict the effect of centerline boundary-layer thickening or streak-like mean-flow distortion on intermittency production, leading to an artificially enhanced transition tendency near the symmetry plane. The experimental heat-flux distribution is also affected by wall thermal response, surface condition, and facility-dependent disturbance environment. Therefore, the validation should be interpreted mainly in terms of the global transition topology and onset tendency, rather than as a point-by-point reproduction of the measured heat-flux field..

Table 1 Freestream conditions

Ma_∞	P_0(Mpa)	T_0(K)	T_w(K)	α(°)	Re_∞
6	0.99	482	300	4	0.46×10^7



（a）Intermittency factor distribution of HyTRV obtained using the improved *k–ω–γ* model

（b）Experimental data provided by the National Key Laboratory of Aerospace Aerodynamics.

Fig. 1 Comparison between numerical predictions and experimental measurements for the HyTRV configuration.

2.2.2 HIFiRE-5

To further assess the applicability and predictive reliability of the improved *k–ω–γ* transition model across different geometries and freestream conditions, the HIFiRE-5 vehicle is selected as an additional validation case. The HIFiRE-5 configuration used in the simulations corresponds to a 0.381-scale configuration employed by Juliano et al. [30] in the Boeing/AFOSR Mach 6 wind tunnel experiments, with the corresponding freestream conditions listed in Table 2. A comparison between the numerical results and experimental data is shown in Fig. 2.

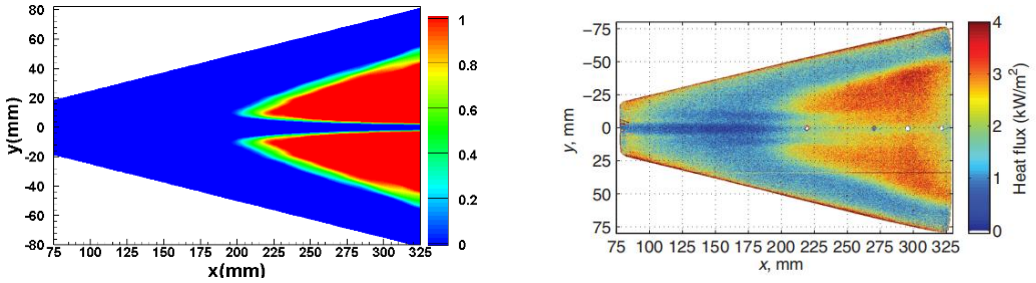
In Fig. 2, panel (a) presents the distribution of the intermittency factor γ, where a value of 0 denotes laminar flow and 1 represents fully turbulent flow, providing a direct visualization of the spatial extent of the transition regions; panel (b) shows the wall heat-flux distribution. Since the wall heat flux typically exhibits a marked increase downstream of transition, the heat-flux distribution can also serve as an important indirect criterion for identifying the onset location and the configuration of the transition front.

The predicted main transition region is located at approximately $x \approx 200$ mm, showing good agreement with the experimental trend. The computed transition front also reproduces the characteristic double-lung-shaped topology observed in the experiment, indicating that the improved *k–ω–γ* transition model can accurately capture the primary transition features of the HIFiRE-5 configuration under hypersonic conditions. Some local discrepancies are still observed near the leading edge, which may be related to the different transition indicators used in the simulation and experiment, namely the modeled intermittency factor and the measured wall heat-flux response. In addition, factors such as leading-edge condition, wall-temperature

nonuniformity, and freestream disturbance level may influence the early heat-flux distribution. Overall, the comparison confirms the predictive capability and engineering applicability of the present model for boundary-layer transition prediction on complex three-dimensional hypersonic geometries.

Table 2 Freestream conditions

Ma_∞	Re_∞(/m)	T_∞(K)	ρ_∞(kg/m^3)	T_w(K)	Tu_∞(%)
5.8	6.1×10^6	51.4	0.024	300	0.1



（a）Distribution of the intermittency factor γ for HIFiRE-5 computed using the improved k–ω–γ model

（b）Experimental trend from Ref. [30]

Fig. 2 Comparison between numerical predictions and experimental measurements for the HIFiRE-5 configuration.

In summary, the successful validation against these two representative three-dimensional configurations demonstrates that the improved k–ω–γ transition model developed in this study can reliably simulate boundary-layer transition phenomena induced by factors such as crossflow instability. This provides a solid data foundation for the subsequent analysis of aerodynamic heating and transition characteristics of derivative configurations based on the HyTRV and HIFiRE-5 configurations.

3 Computational Setup and Parametric Configuration

3.1 Design of Standard Configurations for Hypersonic Transition Studies

3.1.1 Design Concept

This study aims to address the limited generality of existing hypersonic lifting-body transition benchmark configurations and the unclear influence of geometric parameter variations on transition characteristics. By focusing on parametric shape modifications, the work systematically investigates the mechanisms linking subtle geometric deformations to transition features, and analyzes how parametric control affects the flow-field structure and transition behavior of lifting bodies. Specifically, a

new benchmark configuration, named PaTLiB (Parametric Transition Lifting Body) and illustrated in Fig. 3, is first constructed to better reflect the morphology of real vehicles. Its configuration integrates the aerodynamic features of the upper shell of the HyTRV vehicle and the lower shell of the HIFiRE-5 vehicle, and offers three main advantages: (1) it can generate transition regions with multi-modal coupling to emulate realistic flow scenarios; (2) a 100 mm-wide flat-plate region is provided in the midsection of the configuration for unrestricted sensor installation to obtain effective transition data; and (3) it is suitable for parametric studies. The benchmark configuration is dimensioned with a total length of 800 mm, a width of 300 mm, and an upper-half height of 150 mm, with curves 1 and 2 designated as the core parametric variables. Next, a targeted parametric approach is adopted to quantitatively manipulate the vehicle geometry: the concave curvature of the waist region is adjusted by fixing the chord length and varying the central angle (θ), while the convex curvature of the windward surface is modified by changing the aspect ratio (φ) of the circumferential section. Using a control-variable approach, these two curvature features are combined to generate a series of different aerodynamic configurations—for example, PaTLiB-θ20φ6 denotes a configuration with a leeward central angle of 20° and a windward aspect ratio of 6. This allows for a systematic investigation of the effects of waist concavity and windward convexity on transition characteristics. Finally, simulations are conducted for each parametric benchmark configuration using the improved k–ω–γ transition model to predict how subtle variations in waist central angle and windward aspect ratio influence the transition behavior of lifting bodies, thereby providing direct theoretical support for precise design and active control of transition in engineering practice.

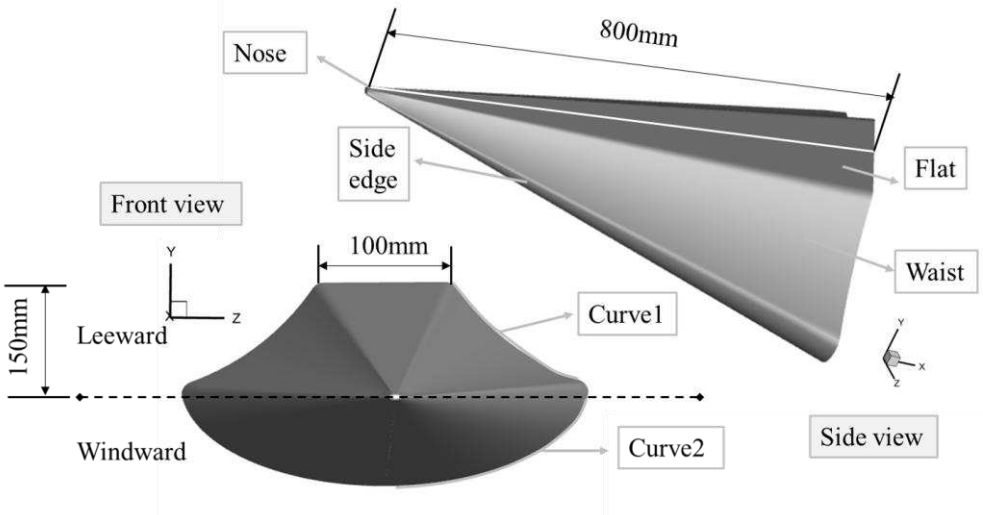
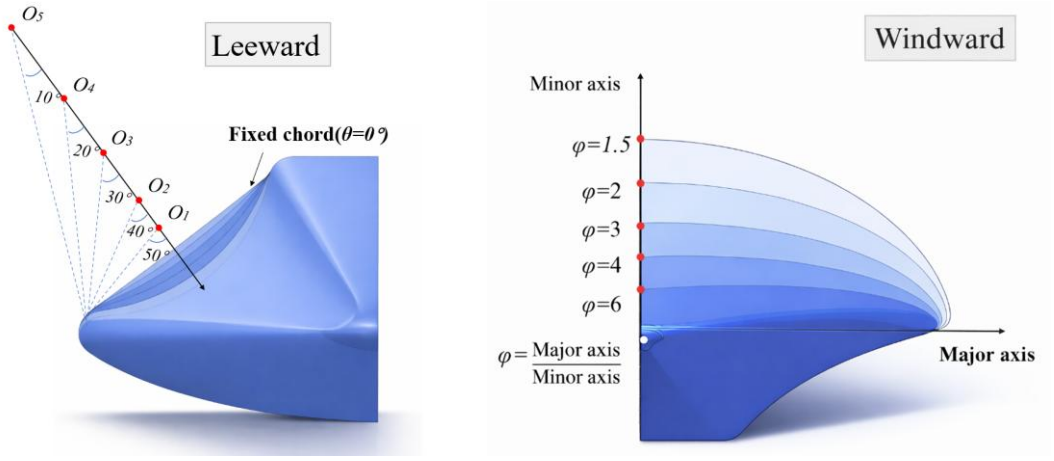


Fig. 3 Schematic diagram of the configuration

3.1.2 Details of Parametric Deformation

In Fig. 4, the parametric geometric deformation method adopted in this study is illustrated in detail. This parametric design approach is based on the cross-sectional shape and enables flexible and continuous control of the vehicle geometry through the introduction of control parameters with clear geometric significance. For the leeward surface, angles such as $\theta 10$ and $\theta 20$ are defined as the central angles corresponding to a fixed reference chord length $\theta 0$, while points O_1–O_5 denote the geometric control points used to define the leeward waist curvature. For the windward surface, $\varphi 3$ and $\varphi 4$ are elliptical shape control parameters, representing the ratio of the major to minor axes of the ellipse; their variation directly affects the flatness and convex curvature of the windward surface, thereby influencing the circumferential pressure gradient, crossflow development, and boundary-layer stability.



(a) Leeward surface parameterized by the central angle θ

(b) Windward surface parameterized by the curvature parameter φ

Fig. 4 Details of Parametric Deformation

3.2 Free-Stream Conditions

To investigate the boundary-layer transition characteristics of lifting bodies under hypersonic conditions, calculations in this study were conducted using representative engineering conditions (Table 3), where the free-stream Mach number Ma_∞, flight altitude H, Reynolds number Re_∞, static pressure p_∞, temperature T_∞, wall temperature T_w, and angle of attack α all fall within the representative ranges of hypersonic cruise missions.

Table 3 Free-Stream Conditions

Ma_∞	H(Km)	Re_∞/E6	$p_\infty(p_a)$	T_∞(K)	T_w(K)	α(°)

		（/m）				
6	24	6.7	2971.75	220.56	300	0

3.3 Grid Independence Verification

Since the geometric configuration constructed in this study is symmetric, a half-configuration was used in the numerical simulations to improve computational efficiency and reduce resource consumption. Structured grids were adopted due to their high cell quality and good wall conformity. During grid generation, local refinement was applied in regions with significant flow gradients, mainly including areas where oblique shocks may occur and the vicinity of boundary layers. These regions are typically associated with strong curvature and large gradients in physical quantities, and refinement is essential for accurately capturing flow structures and ensuring the precise resolution of disturbance modes within the boundary layer. The final grid topology and computational domain are illustrated in Fig. 5.

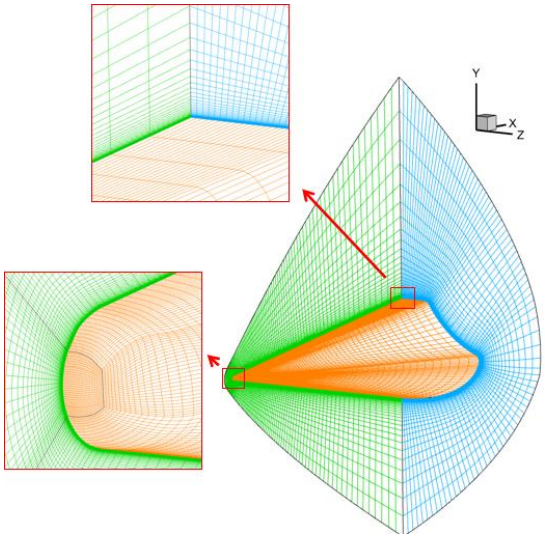


Fig. 5 Grid topology and schematic of the computational mesh

To eliminate the potential influence of grid density on the computational results and ensure that the calculation accuracy is not affected by inappropriate discretization, a systematic grid independence verification was conducted in this study. During this process, three sets of structured grids with total cell counts of 1.16 million, 0.63 million, and 0.43 million were tested, with the specific number of nodes in the streamwise, circumferential, and wall-normal directions detailed in Table 4. To accurately capture the flow details within the boundary layer, the wall-grid Reynolds number of all grids was maintained at $Re_{\Delta x} \approx 10$, and the wall-normal grid growth ratio within the boundary layer was kept below 1.05. The formula for $Re_{\Delta x}$ is given as follows:

$$Re_{\Delta x} = \frac{\rho U \Delta x}{\mu} \tag{3.1}$$

Here, ρ refers to the local fluid density, U refers to the local fluid velocity, Δx represents the grid spacing in the mainstream direction, and μ denotes the dynamic viscosity.

By comparing the wall heat-flux distributions at the *R2* region for the three grid sets (Fig. 6), it can be observed that Grid 1 (1.16 million cells) and Grid 2 (0.63 million cells) predict highly consistent transition onset locations, transition-zone lengths, and wall heat-flux characteristics, indicating that further grid refinement beyond this density has negligible effect on the results. In contrast, Grid 3 (0.43 million cells) exhibits larger numerical dissipation, causing an unphysical premature transition. Considering both numerical accuracy and computational cost, Grid 2 ensures accurate capture of key physical features while providing higher computational efficiency, and is therefore adopted for all subsequent simulations.

Table 4 Grid parameters for each mesh set

Grid	Number of grid nodes			y(mm)	y^+	Total number (million)
	streamwise	circumferential	normal directions			
1	119	118	85	8×10^{-4}	0.4	1.16
2	99	88	75	2×10^{-3}	1	0.63
3	89	73	70	4×10^{-3}	2	0.43

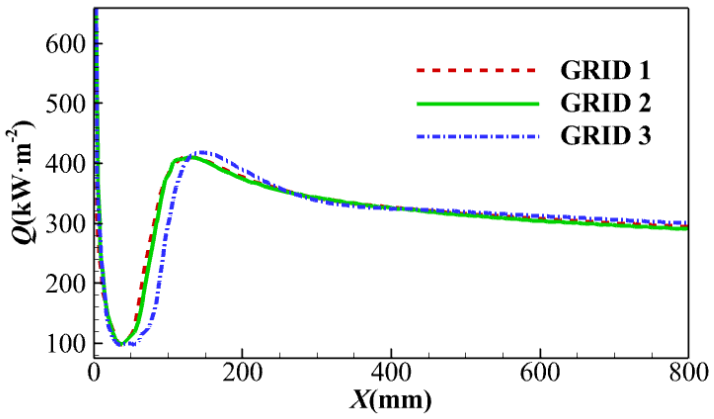


Fig. 6 Comparison of heat flux density on the wall surface of different grids at *R2* region

4 Results and analysis

4.1 Basic flow field and transition characteristics

The transition behavior observed on the PaTLiB configuration can be interpreted from the perspective of curvature-induced pressure gradients and their influence on instability competition within the boundary layer.

Geometric curvature modifies the circumferential pressure distribution, which in turn generates crossflow motion and redistributes the boundary-layer thickness. These effects directly alter the relative amplification of first-mode, second-mode, crossflow, and streamwise-vortex instabilities, ultimately determining the topology of the transition front.

First, the configuration with PaTLiB-θ20φ2 is selected as a representative case, and its flow-field structure and transition characteristics are analyzed to establish a fundamental understanding of the flow details associated with the configuration designed in this study. Fig. 7 presents the distributions of pressure and Mach number for the PaTLiB-θ20φ2 configuration. Five cross sections are extracted at equal intervals within the range of x=100mm to x=700mm. The first four cross sections are rendered using Mach number contours, while the last cross section (x = 700 mm) and the vehicle surface are rendered using the nondimensional pressure P/P_∞. It is evident that the circumferential pressure distribution is highly non-uniform, with a low-pressure region forming over the dorsal flat plate and the bottom main-body region, whereas localized high-pressure regions appear near the side edges and the waist, with the highest pressure occurring in the vicinity of the side edges. This modification of the pressure gradient fundamentally alters the original flow structure under hypersonic freestream conditions. Owing to the larger local flow deflection, the shocks near the side edges are stronger and located closer to the surface. As a result, the post-shock pressure increases, and a closer shock–surface interaction leads to a higher-pressure level. Consequently, the pressure near the side edges exceeds that on the aft and lower-body regions, giving rise to a circumferential pressure gradient.

This pressure gradient drives the flow to shift from the side edges toward the bottom and dorsal regions, generating a crossflow velocity component. The flows originating from the upper and lower parts eventually converge along the centerline of the dorsal and bottom surfaces, leading to boundary-layer thickening near the centerline and the formation of mushroom-shaped streak-like structures. In addition, a localized

low-pressure region is observed near the junction between the side edge and the waist region (highlighted by the white circle). The formation of this localized low-pressure zone is associated with the local curvature variation of the configuration at this location. Furthermore, this region gradually expands as the aspect ratio decreases, as discussed in detail in Fig. 13. A comprehensive analysis of this phenomenon is provided in Section 0.

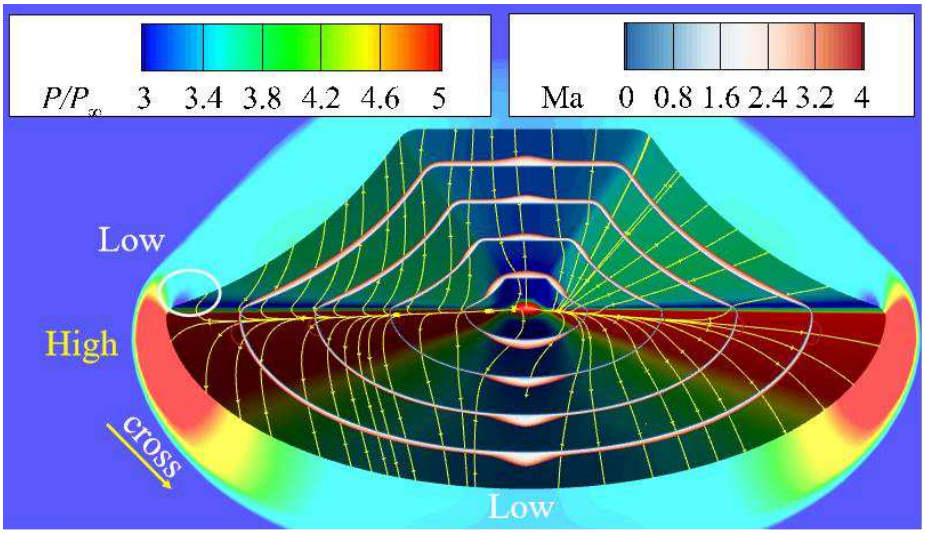


Fig. 7 Surface pressure, wall streamlines, and Mach-number distributions for the PaTLiB-θ20φ2 configuration.

Fig. 8 presents the contours of the transition intermittency on the windward and leeward surfaces of the configuration. The intermittency factor γ characterizes the local flow state, where $\gamma = 0$ denotes laminar flow, $0 < \gamma < 1$ corresponds to the transitional regime, and $\gamma = 1$ indicates fully developed turbulence. Based on these distributions, distinct transition regions are identified and denoted as *Rx*, with their specific definitions provided below：

R1 denotes the leeward flat-plate region;

R2 corresponds to the leeward waist region;

R3 represents the centerline region on the windward surface;

R4 denotes the regions adjacent to the windward centerline;

and *R5* corresponds to the edge and corner regions of the aft flat-plate surface.

As illustrated in Fig. 8, a well-defined V-shaped transition front develops over the leeward flat-plate region. In contrast, within the leeward waist region, the transition front assumes a cone-like structure, closely resembling that observed on the leeward waist of the HyTRV configuration (see Fig. 1(b)). Notable discrepancies, however, are evident along the leeward symmetry plane. These differences arise from the

replacement of the dorsal ridge in the HyTRV configuration with a flat-plate surface in the present configuration, a geometric modification that induces substantial alterations in the transition pattern.

On the windward surface, the transition front displays a characteristic "double-lung" pattern, closely resembling that observed on the windward surface of the HIFiRE-5 vehicle (see Fig. 2(b)). Compared with HIFiRE-5, however, the transition front in the present configuration extends further toward the side-edge regions. Although the lower-body aspect ratio of the present configuration is identical to that of HIFiRE-5 (2:1), differences in the dorsal geometry and side-edge fillet curvature give rise to fundamentally distinct geometric features, thereby leading to pronounced modifications in the overall transition behavior.

Fig. 9 presents the surface heat-flux distributions. Regions of abrupt heat-flux variation are observed to correlate strongly with the transition locations, underscoring the dominant role of boundary-layer transition in governing surface heat-transfer characteristics. On the leeward surface, the heat flux in the laminar region is approximately 200 $kW \cdot m^{-2}$, while following transition it increases markedly, exceeding 280 $kW \cdot m^{-2}$ in the fully turbulent region. The maximum heat flux occurs within the transitional regime, reaching values of approximately 450 $kW \cdot m^{-2}$. On the windward surface, the laminar heat flux is on the order of 150 $kW \cdot m^{-2}$ and rises to approximately 350 $kW \cdot m^{-2}$ after transition.

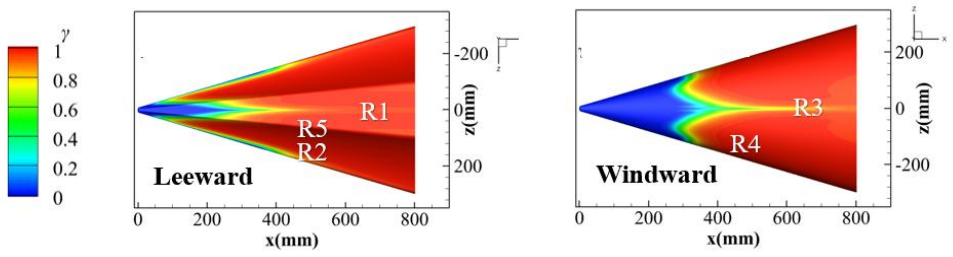


Fig. 8 Intermittent factor distribution cloud map

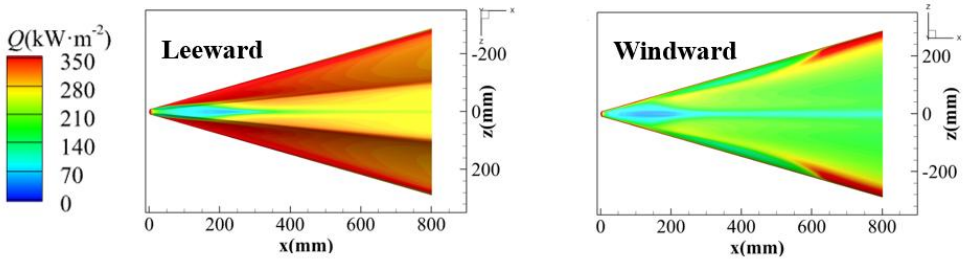


Fig. 9 Wall heat flux distribution contour plot

A quantitative comparison of the surface heat flux in different transition regions

is further conducted, as shown in Fig. 10. The locations of abrupt heat-flux increase in the profiles correspond to the onset of boundary-layer transition. As indicated in Fig. 10, the transition onset locations for regions *R1* to *R5* are located at x=248mm, x=28mm, x=260mm, x=252mm, and x=128mm, respectively. Compared with the other regions, the transition onset in region *R2* occurs significantly earlier. In addition, region *R2* exhibits the highest heat-flux level, with its peak located within the transitional region and reaching approximately 470 $kW \cdot m^{-2}$. When comparing the fully turbulent regions, the heat-flux magnitude follows the order *R2*≈*R4*≈*R5*>*R1*≈*R3*. The turbulent heat flux in regions *R1* and *R3* is only about two-thirds of that in the other regions. In the heat-flux distribution profiles, the streamwise extent of the transitional region is defined as the distance between the peak and the valley of the heat flux within the transitional interval. Based on this definition, it is observed that transition in region *R2* develops rapidly, with a streamwise transitional length of approximately 70mm, whereas the transitional lengths in the other regions range from 120 to 200mm.

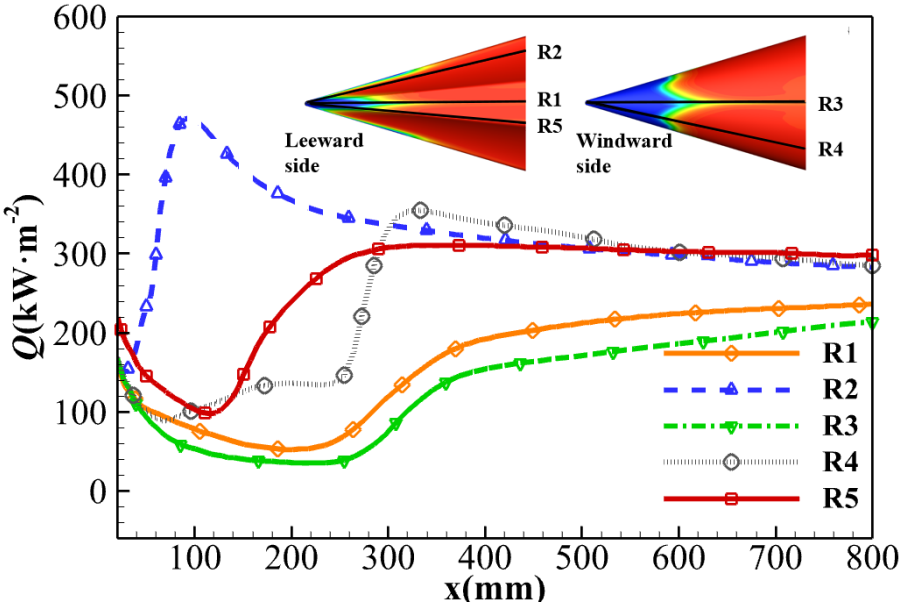
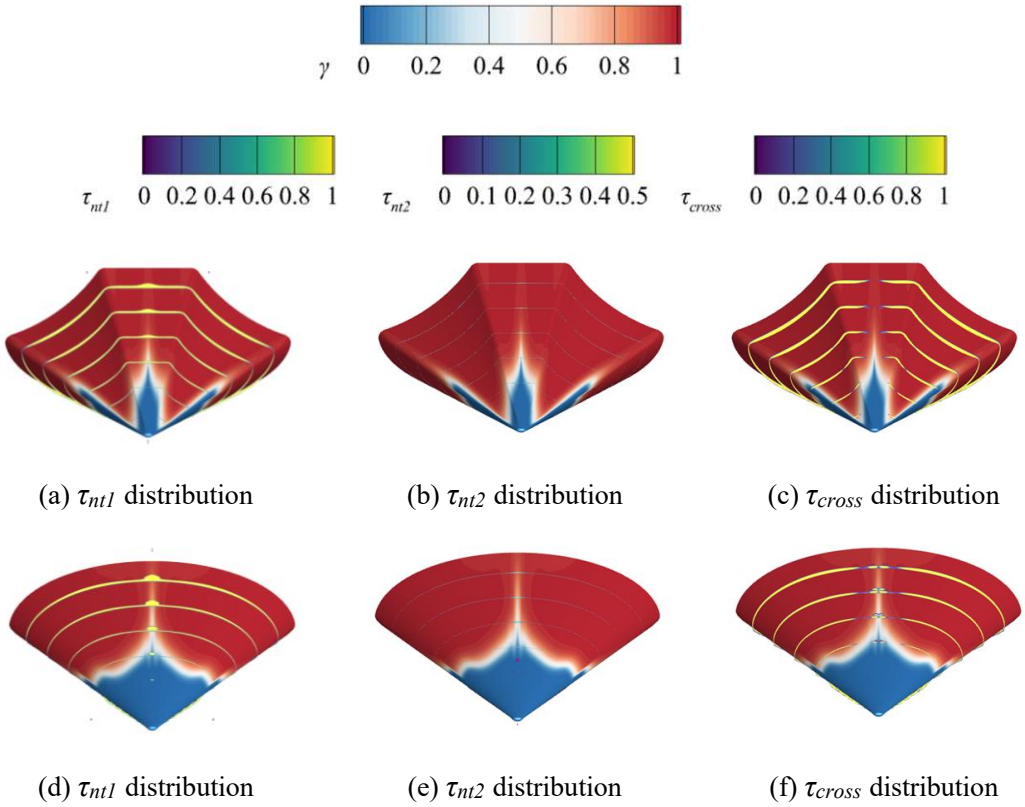


Fig. 10 Streamwise distributions of wall heat flux in different transition regions.

To elucidate the dominant instability mechanisms involved in the transition prediction process of the employed transition model, Fig. 11 presents the distributions of the time scales associated with first-mode, second-mode, and crossflow disturbances within the boundary layer, as formulated in the k–ω–γ transition framework. These time scales are denoted as τ_{nt1}, τ_{nt2}, *and* τ_{cross}, respectively. According to the definition of τ_{nt1}, this time scale is directly linked to the local boundary-layer thickness and therefore increases in regions where the boundary layer is significantly thickened, shown in Fig. 11 (a) and 11(d). In particular, a pronounced mushroom-shaped streak-like structures

develops along the windward centerline, promoting transition in the centerline regions of both the windward and leeward surfaces. The distributions of the second-mode disturbance time scale, shown in Fig. 11 (b) and 11(e), indicate that τ_{nt2} also contributes to transition enhancement in the vicinity of the centerline. Owing to the constraint that τ_{nt2} is activated only in regions where the relative Mach number $|Ma_{rel}|$ exceeds unity, its spatial extent is confined to a thin near-wall layer.

In regions characterized by pronounced crossflow effects—namely, the waist region *R2* and the regions adjacent to the windward centerline on both sides (*R4*)—the distributions of τ_{cross} shown in Fig. 11 (c) and 11(d) indicate that this time scale attains its largest magnitudes and spans the widest spatial extent. This observation provides initial evidence that boundary-layer transition in these regions is predominantly governed by crossflow instability.



(a) τ_{nt1} distribution (b) τ_{nt2} distribution (c) τ_{cross} distribution

(d) τ_{nt1} distribution (e) τ_{nt2} distribution (f) τ_{cross} distribution

Fig. 11 Distribution of τ_{nt1}, τ_{nt2}, and τ_{cross} on the wall boundary layer

To further assess whether transition in regions *R2* and *R4* is predominantly governed by crossflow instability during the prediction process, Fig. 12 presents the contours of the crossflow Reynolds number, Re_{cf}, as a supplementary diagnostic. The crossflow Reynolds number Re_{cf} is widely used to quantify the distribution and intensity of crossflow within the boundary layer, and its formulation is given by

$$Re_{cf} = \frac{\delta_{0.1} w_{max}}{\nu_e} \tag{4.1}$$

Here, $\delta_{0.1}$ denotes the wall-normal distance at which the local crossflow velocity satisfies w/w_{max} =0.1, where w_{max} is the maximum crossflow velocity within the boundary layer, and ν_e is the molecular kinematic viscosity evaluated at the boundary-layer edge. A larger value of the crossflow Reynolds number Re_{cf} indicates a stronger crossflow effect. Based on experimental investigations of supersonic boundary layers over circular cones by Reed et al. [31]and Malik et al.[32], the critical range of the crossflow Reynolds number for transition onset in supersonic flows has been calibrated to lie between 250 and 450. By jointly examining the intermittency factor γ and the contours of the crossflow Reynolds number Re_{cf} in Fig. 12, it is found that the values of Re_{cf} at the transition onset locations in the leeward region *R2* and the windward region *R4* fall within the range of 250–450. This observation is in close agreement with the aforementioned experimental criteria, suggesting that transition in regions *R2* and *R4* is predominantly governed by crossflow instability. It should be noted, however, that owing to flow symmetry, the crossflow velocity approaches zero near the centerline, indicating weak local crossflow intensity. Nevertheless, relatively large values of Re_{cf} are still observed in the vicinity of the windward centerline. According to the definition of Re_{cf}, this behavior results from the locally increased boundary-layer thickness in the centerline region. As a result, although the crossflow velocity is small, the corresponding crossflow Reynolds number can still attain relatively high values. This observation indicates that the identification of crossflow-dominated transition should be based on a combined assessment of both the crossflow Reynolds number and the crossflow velocity. Specifically, in addition to Re_{cf} exceeding the critical threshold of 250, the crossflow velocity w must also reach a certain magnitude to effectively trigger crossflow instability.

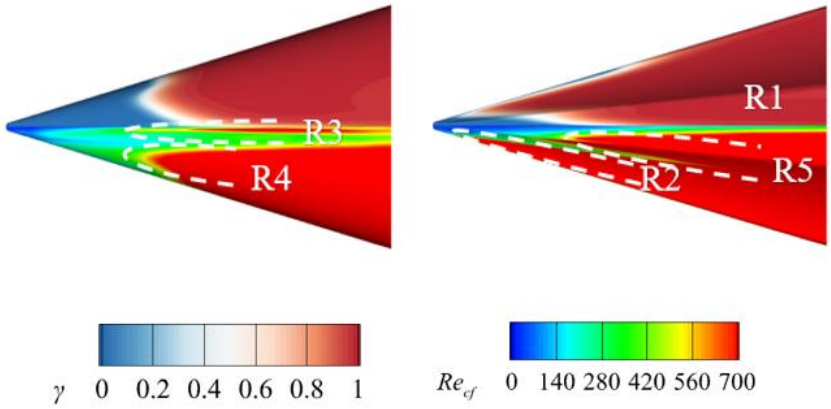


Fig. 12 Configuration wall Re_{cf} and γ distribution contour plot

These observations highlight that the transition behavior over the PaTLiB configuration arises from the interaction of multiple disturbance mechanisms rather than from a single dominant instability mode.

The spatial distribution of instability time scales reveals a clear correspondence between the local geometric environment and the dominant instability mechanism. Regions where the boundary layer thickens due to flow convergence favor the amplification of streamwise-vortex-type disturbances, whereas regions subjected to strong circumferential pressure gradients promote crossflow instability. In contrast, in areas with relatively weak crossflow but high local Mach number, the classical first- and second-mode instabilities remain active.

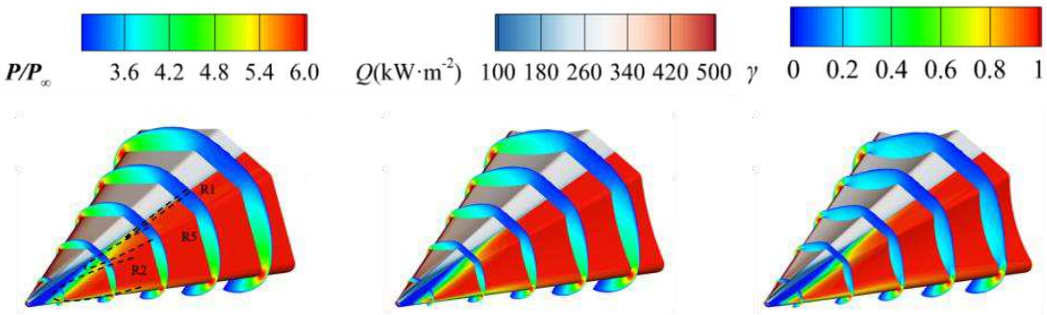
This spatial redistribution of instability dominance results in a heterogeneous transition topology across the vehicle surface. Specifically, the centerline regions are characterized by boundary-layer thickening and streak-like mean-flow structures, which enhance low-frequency non-modal disturbance growth and modify the local modal instability environment. In contrast, the waist and lateral regions are mainly affected by pressure-gradient-driven crossflow, while the edge regions are more strongly influenced by first- and second-mode modal instabilities. These results suggest that geometric curvature acts as an effective control parameter that reorganizes instability competition in three-dimensional hypersonic boundary layers.

4.2 The influence of changes in geometric parameters on transition patterns

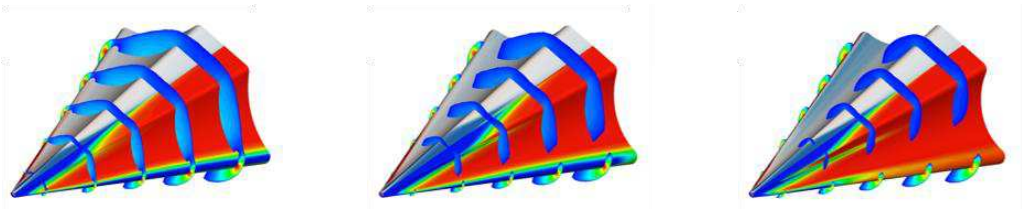
To examine the influence of geometric parameter variations on the flow characteristics and transition behavior, a systematic parametric study is conducted in this subsection. The configuration PaTLiB-θ20φ3 is selected as the baseline case. Two

key geometric parameters are investigated with respect to their effects on boundary-layer transition. First, under the constraint of a fixed aspect ratio φ, the influence of variations in the leeward central angle θ on the development of flow instabilities is analyzed. Second, with the leeward central angle θ held constant, the effect of changes in the aspect ratio φ on transition behavior is examined. As an initial step, the distributions of the wall intermittency factor $\gamma$and surface heat flux Q for six different central angles (θ=0°–50°) are presented, together with contours of the nondimensional pressure P/P_∞ on several equally spaced cross sections, as shown in Fig. 13. Because variations in the central angle primarily modify the curvature of the leeward waist region, the flow features and transition behavior on the leeward surface are examined first.

As illustrated in Fig. 4, the central angle primarily controls the concave curvature of the leeward waist region, with larger values of θ corresponding to stronger concave curvature. As shown in Fig. 13 (a)~(f), increasing θ progressively reduces the overall pressure level on the leeward surface and leads to a pronounced decrease in the surface heat flux Q within the waist region (*R2*). Concurrently, the transition behavior over the configuration surface undergoes notable changes. The transition onset in the edge–corner region of the leeward flat plate (*R5*) is gradually delayed with increasing θ, except for a slight upstream shift observed at θ=50°. In contrast, the transition front in the waist region (*R2*) transforms from a single-cone structure for θ=0° – 30° to a double-cone pattern for θ=40°–50°. This behavior indicates that increasing concave curvature modifies the circumferential pressure distribution in the waist region, thereby strengthening crossflow and altering the associated instability amplification. As a result, the transition topology reorganizes from a single-cone structure to a double-cone pattern, reflecting a transition from purely crossflow-dominated instability toward a coupled crossflow–streak-like structures regime.



（a）θ0　　（b）θ10　　（c）θ20



（d）θ30　　（e）θ40　　（f）θ50

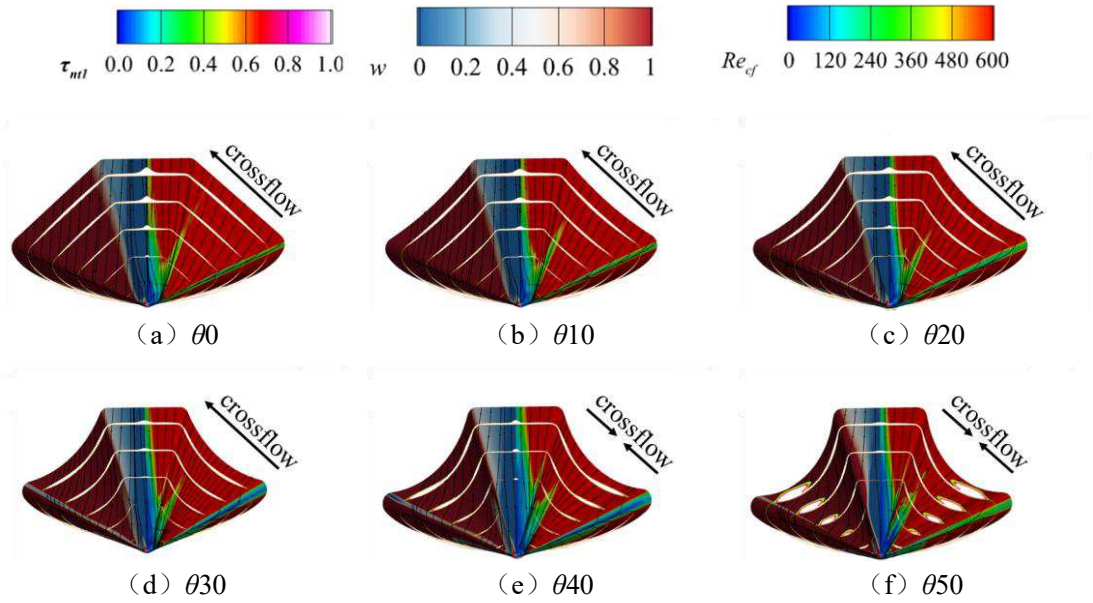
Fig. 13 Cloud charts of γ, Q, and P/P_∞ on the leeward side with different central angles

To elucidate the underlying mechanisms, Fig. 14(a)~(f) presents wall-streamline patterns, crossflow-related parameters, and the first-mode time-scale distribution τ_{nt1} on selected cross sections for different central angles. The flat-plate region is examined first. As shown in Fig. 13, increasing the central angle gradually reduces the pressure level in the waist region, thereby decreasing the pressure difference between the waist and flat-plate regions. Correspondingly, Fig. 14 shows that the crossflow over the flat-plate region is progressively weakened, and the streak-like structures near the flat-plate centerline become less pronounced at $\theta = 50°$. However, the transition onset in region *R5* shifts slightly upstream compared with that at $\theta = 40°$. This behavior is associated with the further reduction of waist pressure, which becomes lower than that over the flat plate and causes a reversal of the original crossflow direction. As a result, the local crossflow intensity in region *R5* is enhanced. Since crossflow can promote first-mode amplification [33], the transition onset in *R5* is advanced. Therefore, the transition behavior in this region cannot be attributed solely to first-mode instability; instead, it reflects the combined influence of first-mode instability and pressure-gradient-induced crossflow.

The leeward waist region is then analyzed. As inferred from Fig. 14, the initial single cone-shaped transition front is mainly associated with crossflow-induced transition driven by relatively strong crossflow velocities. With increasing central angle, the low-pressure region marked in Fig. 7 expands, further reducing the local pressure level in the waist region. This pressure redistribution modifies the original flow structure. The initially unidirectional flow pattern, from the side edge toward the waist and then toward region *R5*, is replaced by a bifurcated flow pattern. One branch develops from the side edge toward the waist, while the other moves from region *R5* toward the waist. Consequently, the transition front evolves from a single cone-shaped pattern into a double cone-shaped pattern. The wall-streamline distributions further show that the two branches converge near the junction between the waist and the side edge. At $\theta = 50°$, a relatively strong streak-like structure forms in this region, leading to a pronounced modification of the transition front in *R2*. Thus, the transition behavior

in the waist region changes from being primarily crossflow-dominated to being influenced by the interaction between crossflow and streak-like mean-flow distortion. In addition, the transition onset near the side edge first shifts downstream and then moves upstream as the central angle increases, which is related to the non-monotonic variation of crossflow intensity and crossflow velocity near the side edge.

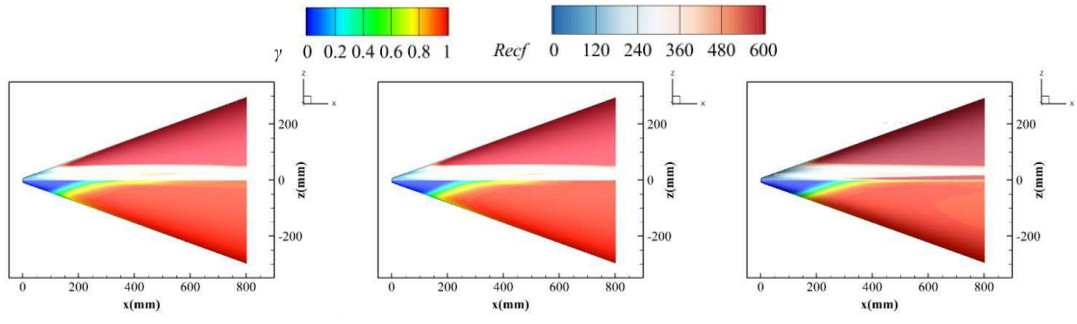
Fig. 15 further shows the intermittency factor γ and crossflow Reynolds number Re_{cf} on the windward surface for representative central-angle cases. Since the central angle mainly modifies the leeward-side geometry, its influence on the windward surface is limited. Only a slight downstream shift of the transition onset is observed, while the crossflow intensity remains nearly unchanged. This indicates that central-angle variation has a weak effect on windward-side transition behavior.



（a）θ0　（b）θ10　（c）θ20

（d）θ30　（e）θ40　（f）θ50

Fig. 14 Leeward-Flow Characteristics under Different Central angles



（a）θ0　（b）θ10　（c）θ20

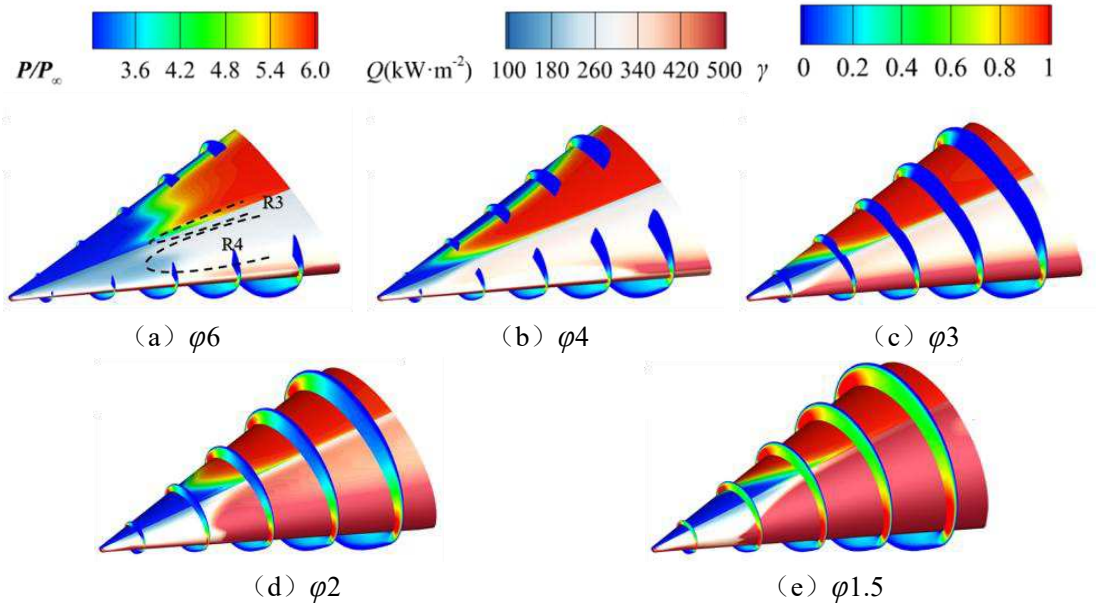
Fig. 15 Transition characteristics on the windward surface for different central angles

To investigate the influence of the aspect ratio φ on windward-side flow and transition behavior, Fig. 16 (a)~(e) presents the distributions of the intermittency factor, wall heat flux, and pressure contours for different φ values. Since the aspect ratio

mainly modifies the windward geometry and has little influence on the leeward-side transition, the following discussion focuses on the windward surface. As shown in Fig. 16 , even small changes in φ lead to evident differences in both transition-front topology and transition onset location. With decreasing φ, namely increasing windward convex curvature, the transition onset near the side edge and in region *R4* varies non-monotonically, and the transition front alternates between an "M-shaped" pattern for φ = 6, 4, and 2 and a "V-shaped" pattern for φ = 3 and 1.5.

The mechanism can be further clarified from the crossflow-related quantities and wall-streamline distributions in Fig. 17. For large φ values, such as φ = 6 and 4, the windward surface is relatively flat, resulting in a more uniform circumferential shock structure and a small pressure difference between the side edge and the centerline region *R3*. Consequently, the crossflow velocity in region *R4* remains weak, and the transition behavior is mainly associated with first-mode instability, leading to an M-shaped transition front. As φ decreases, the windward surface becomes fuller and closer to an elliptical shape. The post-shock pressure then becomes higher near the side edge and decreases toward the centerline, producing a stronger circumferential pressure gradient. This pressure gradient enhances both the crossflow Reynolds number and the crossflow velocity, and the influence of crossflow gradually extends from the lateral region toward *R4*. As a result, crossflow effects become increasingly important, and the transition front develops into a V-shaped pattern.

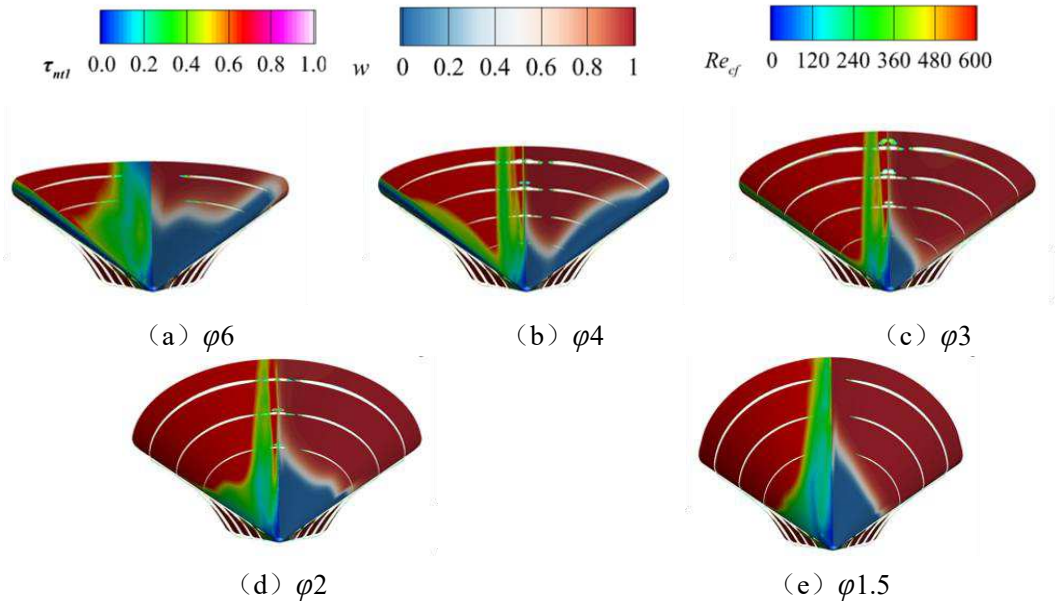
However, this variation is not strictly monotonic. At φ = 2, the wall-streamline pattern indicates a local weakening of crossflow near the side edge, which delays transition in that region and causes the transition front to return to an M-shaped pattern. When φ is further reduced to 1.5, crossflow again expands from the side edge toward *R4*, affecting a broader windward-surface region and producing a V-shaped transition front. It should also be noted that a large Re_{cf} alone does not necessarily indicate crossflow-dominated transition. For cases such as φ= 6–3, the crossflow velocity remains relatively low, and transition in *R4* is still mainly influenced by first-mode instability. Only when both Re_{cf} and crossflow velocity become sufficiently large does the dominant disturbance mechanism gradually shift from first-mode instability to crossflow-dominated transition.



（a）φ6　　（b）φ4　　（c）φ3

（d）φ2　　（e）φ1.5

Fig. 16 Flow, Heat Flux, and Pressure on Windward Surfaces with Varying Axis Ratios



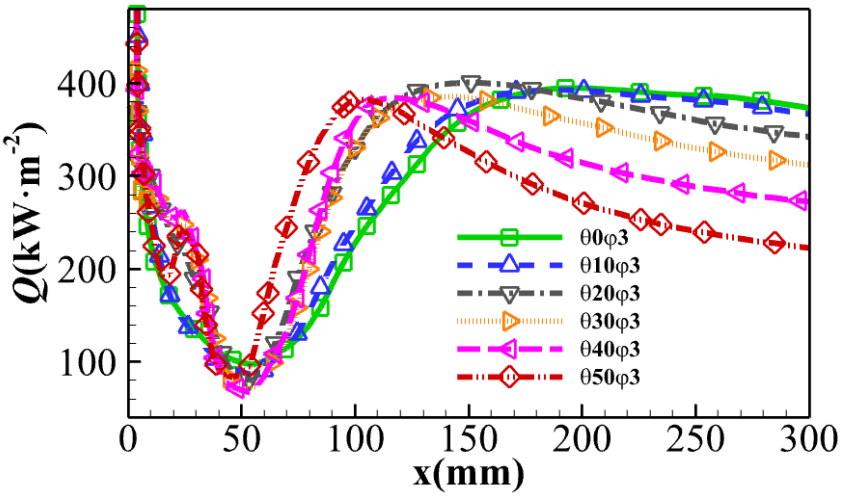
（a）φ6　　（b）φ4　　（c）φ3

（d）φ2　　（e）φ1.5

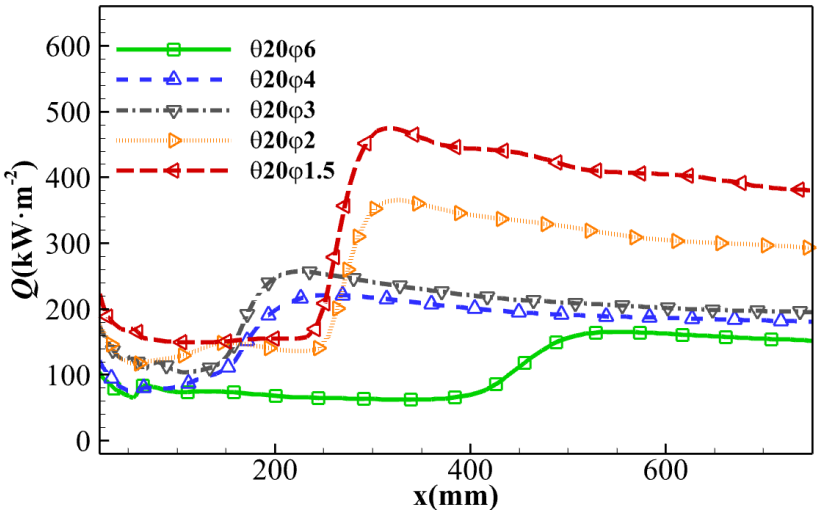
Fig. 17 Windward-Flow Characteristics under Different Axis Ratios

Because even small variations in the configuration parameters lead to pronounced changes in the transition-front patterns, and the surface heat-flux density Q is closely coupled with boundary-layer transition, a detailed analysis of the heat-flux response is conducted. Given that variations in concave curvature (θ) and convex curvature (φ) primarily affect regions *R2* and *R4*, respectively, these two regions are selected as the focus of the analysis. The influence of curvature variations on the wall heat-flux density is examined by extracting characteristic streamwise profiles (see the inset of Fig. 10), and the corresponding results are presented in Fig. 18.

As shown in Fig. 18 (a), increasing the concave curvature in the waist region leads to a reduction in shock strength, accompanied by a progressive decrease in the turbulent heat-flux density downstream of transition. For the case of θ=0°, the turbulent heat flux reaches approximately 306 kW·m^{-2}, whereas it decreases to about 179 kW·m^{-2} when the central angle is increased to θ=50°. According to the definition of the transition-zone length introduced in Sec. 4.1, variations in concave curvature not only modify the magnitude of the post-transition turbulent heat flux but also affect the streamwise extent of the transition region. As illustrated in Fig. 18 (a), the transition onset locations remain nearly unchanged among the different curvature cases, occurring at approximately x≈50mm (quantitative data for all parametric cases are summarized in Table 5). However, with increasing concave curvature, the transition-region length decreases progressively from about 152 mm to approximately 94 mm, indicating an accelerated transition process. Fig. 18 (b) presents the streamwise distributions of windward-surface heat-flux density for different convex curvatures. For the case with relatively small convex curvature (φ=6), the transition onset is located relatively far downstream, as shown in Fig. 17 (a), and the post-transition turbulent heat-flux density remains low, reaching only about 148 kW·m^{-2}. With increasing convex curvature, under the φ=4 and 3 conditions, the transition onset advances markedly due to the enhanced influence of crossflow instability, and the turbulent heat-flux density downstream of transition increases accordingly. As the convex curvature is further increased, the crossflow intensity weakens, and the transition onset locations for φ=2 and 1.5 shift slightly downstream, consistent with the observations in Fig. 17. Nevertheless, the post-transition turbulent heat-flux density continues to rise, with a substantially increased growth rate, reaching approximately 379 kW·m^{-2} in the fully turbulent region for the φ=1.5 case.



(a) Concave curvature



(b) Convex curvature

Fig. 18 Streamwise heat-flux variations under different concave and convex curvatures.

Table 5 Detailed data table of transition for each section under parameterized changes

Parametric	configuration	Onset of transition （mm）	Extent of transition (mm)	Peak heat flux (kW • m^{-2})	Turbulent heat flux (kW • m^{-2})
（concave） Central angle	*θ0φ3*	56	152	394	306
	θ10φ3	54	146	392	304
	θ20φ3	53	111	400	296
	θ30φ3	52	91	385	269
	θ40φ3	50	67	384	227
	θ50φ3	49	57	381	179
（convex） Ratio of major and minor axes	*θ20φ6*	432	94	163	148
	θ20φ4	69	172	219	180
	θ20φ3	124	91	256	194
	θ20φ2	258	63	365	288
	θ20φ1.5	251	62	474	379

5 Conclusions

This study examined curvature-related transition behavior in a three-dimensional hypersonic lifting-body configuration using numerical simulations based on an instability-sensitive *k–ω–γ* transition modeling framework. By independently varying concave and convex surface curvature, the influence of geometric curvature on crossflow development, instability competition, and transition-front organization was systematically investigated. The main observations obtained from the present model-based analysis are summarized as follows.

(1) The numerical results show that transition over the lifting-body configuration is influenced by first-mode, second-mode, and crossflow instabilities, together with non-modal streamwise streaks associated with boundary-layer thickening. While the first three mechanisms are explicitly represented by the instability time scales in the transition model, the streaks are reflected through the resulting mean-flow distortion. Their distribution is mainly controlled by curvature-induced circumferential pressure gradients, which drive crossflow motion and alter the boundary-layer thickness.

(2) Increasing concave curvature in the leeward waist region alters the circumferential pressure field and modifies the crossflow structure within the boundary layer. The predicted transition front evolves from a single-cone topology to a double-cone pattern. Within the present modeling framework, this behavior is consistent with

a transition scenario in which pressure-gradient-induced crossflow interacts with streak-like mean-flow distortion associated with boundary-layer thickening.

(3) Variations in convex curvature on the windward surface lead to non-monotonic changes in the predicted transition location and produce alternating “M-shaped” and “V-shaped” transition fronts. The simulation results indicate that these changes are associated with variations in crossflow intensity and the relative importance of modal instabilities within the boundary layer.

Overall, the present results suggest that geometric curvature may act as an important parameter influencing instability interaction and transition-front organization in three-dimensional hypersonic boundary layers. Through its effect on the circumferential pressure distribution, crossflow intensity, and boundary-layer-thickness redistribution, curvature modifies the local disturbance-amplification environment and thereby alters the topology of the transition front. These observations provide a physical interpretation of curvature-related transition behavior and may offer guidance for transition prediction and aerodynamic design of future hypersonic lifting vehicles.

Acknowledgments

The authors acknowledge the computing resources provided by the High-Performance Computing Public Platform of Central South University, China.

Fundings

This work was supported by the National Natural Science Foundation of China (Grant No. U2541236), the Science and Technology Innovation Plan Project Program of Hunan Province, China (Grant No. 2024RC3016), the Natural Science Foundation of Hunan Province, China (Grant Nos. 2025JJ50017 and 2025JJ50220), and the National Natural Science Foundation of China-Fundamental Science Center Project (Grant No. 52388102).

Author declarations

The authors have no conflicts to disclose.

Author Contributions

Yatian Zhao: Conceptualization (equal); Methodology (equal); Writing-review & editing(equal). Xianda Zeng: Software (equal); Formal Analysis (equal); Writing-original Draft (equal). Jian Luo: Resources (equal); Methodology (equal); Writing-review & editing(equal). Fanzhi Zeng: Validation (equal); Writing-review & editing(equal). Ze Pang： Writing-review & editing(equal). Hongkang Liu: Project administration (equal); Supervision (equal).

Data availability

Data are available from the corresponding author upon reasonable request.

References

[1] Ullah, H., Qiu, H., Yu, G., et al., "Exploring the Boundary Layer Transition of Hypersonic Flow over a Compound Delta Wing," *Physics of Fluids*, Vol. 36, No. 3, 2024.
https://doi.org/10.1063/5.0202268

[2] Hufgard, F., Duernhofer, C., Fasoulas, S., et al., "Novel Heat Flux Controlled Surface Cooling for Hypersonic Flight," *Scientific Reports*, Vol. 13, No. 1, 2023, pp. 13109.
https://doi.org/10.1038/s41598-023-40281-8

[3] Kim, J., Nam, J., Hur, J., et al., "Experimental Study of Nose-Tip Bluntness Effects on Hypersonic Boundary-Layer Transition in a Shock Tunnel," *Scientific Reports*, Vol. 15, No. 1, 2025, pp. 38301.
https://doi.org/10.1038/s41598-025-22323-5

[4] Chen, J., Yi, S., Li, X., et al., "Theoretical, Numerical and Experimental Study of Hypersonic Boundary Layer Transition: Blunt Circular Cone," *Applied Thermal Engineering*, Vol. 194, 2021, pp. 116931.
https://doi.org/10.1016/j.applthermaleng.2021.116931

[5] Tu, G., Chen, J., Yuan, X., et al., "Progress in Flight Tests of Hypersonic Boundary Layer Transition," *Acta Mechanica Sinica*, Vol. 37, No. 11, 2021, pp. 1589–1609.
https://doi.org/10.1007/s10409-021-01153-4

[6] Li, Z., Yu, H., Huang, B., et al., "The Hypersonic Boundary-Layer Transition: A Perspective from System Design," *Acta Aerodynamica Sinica*, Vol. 39, No. 4, 2021, pp. 26–38.
https://doi.org/10.7638/kqdlxxb-2020.0061

[7] Guo, P., Hao, J., and Wen, C. Y., "Transition Reversal over a Blunt Plate at Mach 5," *Journal of Fluid Mechanics*, Vol. 1005, 2025, Paper. A5.
https://doi.org/10.1017/jfm.2024.1236

[8] Li, X., Yu, J., and Wu, J., "Hypersonic Boundary-Layer Instability Response to Nose-Tip Distributed Roughness Elements," *AIAA Journal*, Vol. 63, No. 12, 2025, pp. 5136–5152.
https://doi.org/10.2514/1.j065636

[9] Goparaju, H., and Gaitonde, D. V., "Role of Entropic Instabilities in Laminar–Turbulent Transition on a Blunted Flat Plate," *Physical Review Fluids*, Vol. 7,

No. 10, 2022, pp. 103901.
https://doi.org/10.1103/physrevfluids.7.103901

[10] Paredes, P., Scholten, A., Choudhari, M. M., et al., "Hypersonic Boundary-Layer Transition on Blunted Cones at Angle of Attack," *AIAA Aviation Forum*, 2021, AIAA Paper 2021-2886.
https://doi.org/10.2514/6.2021-2886

[11] Qiu, H., Shi, M., Zhu, Y., et al., "Boundary Layer Transition of Hypersonic Flow over a Delta Wing," *Journal of Fluid Mechanics*, Vol. 980, 2024, pp. A57.
https://doi.org/10.1017/jfm.2024.42

[12] Paredes, P., and Theofilis, V., "Centerline Instabilities on the Hypersonic International Flight Research Experimentation HIFiRE-5 Elliptic Cone Model," *Journal of Fluids and Structures*, Vol. 53, 2015, pp. 36–49.
https://doi.org/10.1016/j.jfluidstructs.2014.11.002

[13] Maslov, A. A., "Hypersonic Boundary Layer Stability and Transition," ITAM Report, ESA/ESTEC TRP Program, 1994–1996.

[14] He, S., and Zhong, X., "Hypersonic Boundary-Layer Receptivity over a Blunt Cone to Freestream Pulse Disturbances," *AIAA Journal*, Vol. 59, No. 9, 2021, pp. 3546–3565.
https://doi.org/10.2514/6.2020-2057

[15] Fedorov, A., "Transition and Stability of High-Speed Boundary Layers," *Annual Review of Fluid Mechanics*, Vol. 43, No. 1, 2011, pp. 79–95.
https://doi.org/10.1146/annurev-fluid-122109-160750

[16] Paredes, P., Gosse, R., Theofilis, V., et al., "Linear Modal Instabilities of Hypersonic Flow over an Elliptic Cone," *Journal of Fluid Mechanics*, Vol. 804, 2016, pp. 442–466.
https://doi.org/10.1017/jfm.2016.536

[17] Moyes, A. J., and Reed, H. L., "Preflight Boundary-Layer Stability Analysis of BOLT Geometry," *Journal of Spacecraft and Rockets*, Vol. 58, No. 1, 2021, pp. 78–89.
https://doi.org/10.2514/1.a34792

[18] Qi, H., Li, X., Yu, C., et al., "Direct Numerical Simulation of Hypersonic Boundary Layer Transition over a Lifting-Body Model HyTRV," *Advances in Aerodynamics*, Vol. 3, No. 1, 2021, pp. 31.
https://doi.org/10.1186/s42774-021-00082-x

[19] Li, X., Xu, B., Huang, G., et al., "Experimental Study on the Boundary Layer Transition of a High-Speed Fin-Cone Configuration," *Advances in Aerodynamics*, Vol. 7, No. 1, 2025, pp. 10. https://doi.org/10.1186/s42774-025-00204-9

[20] Xiang, X., Chen, J., Yuan, X., et al., "Cross-Flow Transition Model Predictions of Hypersonic Transition Research Vehicle," *Aerospace Science and Technology*, Vol. 122, 2022, pp. 107327. https://doi.org/10.1016/j.ast.2022.107327

[21] Menter, F. R., Langtry, R. B., Likki, S. R., et al., "A Correlation-Based Transition Model Using Local Variables—Part I: Model Formulation," *Journal of Turbomachinery*, Vol. 128, No. 3, 2006, pp. 413–422. https://doi.org/10.1115/gt2004-53452

[22] Zhou, L., Yan, C., Hao, Z. H., et al., "Improved k–ω–γ Model for Hypersonic Boundary Layer Transition Prediction," *International Journal of Heat and Mass Transfer*, Vol. 94, 2016, pp. 380–389. https://doi.org/10.1016/j.ijheatmasstransfer.2015.11.048

[23] Zhao, Y., Jianqiang, C., Rui, Z., et al., "Assessment and Improvement of k–ω–γ Model for Separation-Induced Transition Prediction," *Chinese Journal of Aeronautics*, Vol. 35, No. 11, 2022, pp. 219–234. https://doi.org/10.1016/j.cja.2022.05.003

[24] Oz, F., and Kara, K., "Controlling Hypersonic Boundary Layer Transition with Localized Cooling and Metasurface Treatments," *Scientific Reports*, Vol. 14, No. 1, 2024, pp. 15928. https://doi.org/10.1038/s41598-024-66867-4

[25] Wang, L., and Fu, S., "Development of an Intermittency Equation for Modeling Supersonic/Hypersonic Boundary Layer Transition," *Flow, Turbulence and Combustion*, Vol. 87, No. 1, 2011, pp. 165–187. https://doi.org/10.1007/s10494-011-9336-1

[26] Zhou, L., Zhao, R., and Yuan, W., "Application of Improved k–ω–γ Transition Model to Hypersonic Complex Configurations," *AIAA Journal*, Vol. 57, No. 5, 2019, pp. 2214–2221. https://doi.org/10.2514/1.j057609

[27] Zhao, Y., Yan, C., Liu, H., et al., "Assessment of Laminar–Turbulent Transition Models for Hypersonic Inflatable Aerodynamic Decelerator Aeroshell,"

International Journal of Heat and Mass Transfer, Vol. 132, 2019, pp. 825–836. https://doi.org/10.1016/j.ijheatmasstransfer.2018.11.025

[28] Wang, L., and Zhou, L., "Prediction of Aerodynamic Characteristics of Hypersonic Vehicle Using Improved k–ω–γ Transition Model," *Acta Aerodynamica Sinica*, Vol. 39, No. 3, 2021, pp. 51–61. https://doi.org/10.7638/kqdlxxb-2019.0146

[29] Wang, L., and Fu, S., "Modeling Flow Transition in a Hypersonic Boundary Layer with Reynolds-Averaged Navier–Stokes Approach," *Science in China Series G: Physics, Mechanics and Astronomy*, Vol. 52, No. 5, 2009, pp. 768–774. https://doi.org/10.1007/s11433-009-0047-8

[30] Juliano, J. T., Borg, M. P., et al., "Quiet Tunnel Measurements of HIFiRE-5 Boundary-Layer Transition," *AIAA Journal*, Vol. 53, No. 4, 2015, pp. 832–846. https://doi.org/10.2514/1.j053189

[31] Reed, H. L., and Haynes, T. S., "Transition Correlations in Three-Dimensional Boundary Layers," *AIAA Journal*, Vol. 32, No. 5, 1994, pp. 923–929. https://doi.org/10.2514/3.12075

[32] Malik, M. R., Li, F., and Chang, C. L., "Crossflow disturbances in three-dimensional boundary layers: nonlinear development, wave interaction and secondary instability," *Journal of Fluid Mechanics*, Vol. 268, 1994, pp. 1–36. https://doi.org/10.1017/s0022112094001242

[33] Lu, J., Uy, K. C. K., Zhao, R., et al., "On the Receptivity of First and Cross-Flow Modes in Hypersonic Sharp Wing Flows," *Journal of Fluid Mechanics*, Vol. 1021, 2025, p. A18. https://doi.org/10.1017/jfm.2025.10708